Quantitative Anisotropic Damage Mechanism in a Forged Aluminum Alloy Studied by Synchrotron Tomography and Finite Element Simulations

Yang Shen, Thilo F. Morgeneyer, Jérôme Garnier, Lucien Allais, Lukas Helfen, Jérôme Crépin

To cite this version:

Yang Shen, Thilo F. Morgeneyer, Jérôme Garnier, Lucien Allais, Lukas Helfen, et al.. Quantitative Anisotropic Damage Mechanism in a Forged Aluminum Alloy Studied by Synchrotron Tomography and Finite Element Simulations. Advances in Materials Science and Engineering, 2019, 2019, pp.1-12. 10.1155/2019/8739419 . hal-02438293

HAL Id: hal-02438293
https://hal.science/hal-02438293v1

Submitted on 22 Jan 2020

Hindawi
Advances in Materials Science and Engineering
Volume 2019, Article ID 8739419, 12 pages
https://doi.org/10.1155/2019/8739419

Research Article

Quantitative Anisotropic Damage Mechanism in a Forged Aluminum Alloy Studied by Synchrotron Tomography and Finite Element Simulations

Yang Shen,[1,2] **Thilo F. Morgeneyer**,[2] **Jérôme Garnier**,[1] **Lucien Allais**,[1] **Lukas Helfen**,[3,4] **and Jérôme Crépin**[2]

[1] *DEN-Service de Recherche Métallurgique Appliquée, CEA, Université Paris-Saclay, F-91191 Gif-sur-Yvette, France*
[2] *MINES ParisTech, PSL Research University, Centre des Matériaux, CNRS UMR 7633, BP 87, 91003 Evry, France*
[3] *ANKA/Institute for Photon Science and Synchrotron Radiation, Karlsruhe Institute of Technology (KIT), D-76131 Karlsruhe, Germany*
[4] *European Synchrotron Radiation Facility (ESRF), BP 220, F-38043 Grenoble Cedex, France*

Correspondence should be addressed to Yang Shen; yang.shen@edf.fr

Received 10 June 2019; Accepted 9 July 2019; Published 25 July 2019

Guest Editor: Dariusz Rozumek

A highly anisotropic toughness behavior has been revealed on a forged AA6061 aluminum alloy by toughness tests with CT specimens. The toughness values with specimens loaded on the longitudinal direction are larger than that loaded on the transverse direction due to the anisotropic shape and distribution of coarse precipitates induced by the morphological anisotropy of grains during forging process. Synchrotron radiation computed tomography analysis on as-received material and arrested cracks revealed different fracture modes for the two loading configurations. The damage mechanism has been validated by finite element simulations based on the Gurson–Tvergaard–Needleman micromechanical damage model with different sets of damage parameters for the two loading configurations obtained from quantitative void volume fraction analysis on SRCT data, in situ SEM experiments, and SRCT microstructural analysis.

1. Introduction

Aluminum alloys are often used in industrial structures for its light weight, its corrosion resistance [1], and its mechanical properties. Toughness is a crucial mechanical property in the design and use of industrial metal components. The toughness is frequently appeared to be anisotropic for forged aluminum alloys. The study on the anisotropic feature helps engineers to predict the lifetime of industrial parts. The origin of the anisotropy of damage is associated with microstructural anisotropy [2–4].

Several models of anisotropic ductile damage, taking into account the microstructural aspects, exist in the literature. These models are based on either the Gurson micromechanical model [5] or its extension developed by Tvergaard and Needleman (named GTN model) [6] or the Lemaitre phenomenological model [7, 8]. The parameters of the GTN model have been identified by 3D synchrotron laminography by Shen et al. [9] in AA6061 aluminum alloy sheets loaded on the transverse direction. The anisotropic behavior was not taken into consideration in this article. Several authors have modified these models by taking into account the coalescence of anisotropic cavities [10–14] based on the work of Thomason [15]. These studies show an increase in the crack propagation resistance in the case where the cavities (or coarse precipitates) are elongated along the initial loading direction. This anisotropy of the microstructure delays the coalescence of the cavities as the intercavity or interprecipitate distance in the path of the crack is larger. However, a limitation exists in these models: only coalescence by internal necking [15] is taken into account in these models, but the coalescence of microcavity-generated ligament on a second population of the precipitates is frequently observed in this material [16, 17].

In this article, the initial microstructure of the alloy was analyzed by synchrotron radiation computed tomography (SRCT). These observations were carried out at the European Synchrotron Radiation Facility (ESRF) on the ID19 beamline. Samples relating to deformed states correspond to parallelepipeds in CT specimens in the region of ductile tearing. Two loading configurations have been studied: LS and TL. We will discuss later in this article these test configurations. The isotropic GTN damage model was used with two parameter sets to represent each configuration taking into account the initial microstructure of the alloy, the germination of cavities on coarse precipitates, the growth of cavities, and two mechanisms cavity coalescence: coalescence by internal necking and coalescence ligament. Cavity nucleation on a secondary population of precipitates was taken into account leading to coalescence mechanism ligament. The model parameters are determined by experimental analysis. The results were then compared with the experimental curves of fracture toughness tests.

2. Experimental

A forged AA6061 alloy was used in this study whose chemical composition is given in Table 1. The material used was in the T6 temper (solution heat treated at 530°C during 3 h and water quenching and aged at 175°C during 12 h). The heat treatment was defined to obtain the maximum yielding stress. More details on the manufacturing process, the microstructure, and mechanical properties of the material are described in [9, 18].

Table 1: Chemical composition of AA6061 alloy (wt.%).

AA6061	Si	Mg	Fe	Cr	Cu	Mn	Zn	Ti
Wt.%	0.65	1.01	0.24	0.18	0.30	0.09	0.20	0.02

The forging direction, the long transverse direction, and the short transverse direction are referenced to the letters *L*, *T*, and *S*, respectively.

Tensile tests have been performed on smooth round specimens with an initial length of 50 mm and diameter of 10 mm. These tests have been conducted through *L* and *T* loading directions with a loading rate of $10^{-4}\,s^{-1}$.

Toughness tests have been carried out on CT12.5 specimens (Figure 1) to investigate the fracture properties according to the ISO standard [19]. Two loading configurations have been conducted: LS and TL. The first letter represents the loading direction and the second the crack propagation direction. A 2.5 mm precrack was introduced by crack-length-controlled fatigue cycling [20]. Tests were performed on a servohydraulic machine with a loading rate of 8.3 μm/s. At least three tests have been performed in each configuration with only a small dispersion of results.

After being taken in the crack initiation and propagation region on arrested CT specimens by electrical discharge machining [21] (Figure 1), samples were scanned by synchrotron radiation computed tomography (SRCT) installed at beamline ID19 [22] of the European Synchrotron Radiation Facility (ESRF) in Grenoble, France. We followed the methods of Shen et al. described in [9]. We used a monochromatic beam of 19 keV X-ray energy. Volumes were reconstructed from angularly equidistant 2000 projections with an exposure time of each projection of 100 ms. A voxel size of 0.7 μm was chosen. Details of the experimental method and image reconstruction are given in [23, 24].

For image analysis performed on as-received material, the analyzed volume is $700 \times 700 \times 700\,\mu\text{m}^3$ corresponding to the representative elementary volume (REV). Only objects with a size larger than $2.1 \times 2.1 \times 2.1\,\mu\text{m}^3$ are considered. For the analysis of arrested CT samples, after the reconstruction of tridimensional images, cracks were first binarized with the morphological algorithm "connected threshold growing" by using the software *ImageJ* and then analyzed using a "sum along ray algorithm" [2, 25, 26]. A Visualization Toolkit (VTK) software routine was used to render the three-dimensional (3D) datasets and produce the 3D images. The aim was to precisely determine and quantify the local crack characteristics such as opening within the 3D volumes.

3. Experimental Results

3.1. Microstructure. Figure 2 shows the microstructure of the as-received material obtained by 3D SRCT analysis. Two types of precipitates at the micrometer scale are present in this material: coarse Mg_2Si and iron-rich intermetallics [18, 27] with, respectively, their volume fraction of $0.43 \pm 0.11\%$ and $0.59 \pm 0.15\%$. Little porosity can be observed with volume fraction less than 0.05%.

The granular structure of the material has been analyzed by SRCT on the gallium-wetted sample. In fact, when liquid gallium is brought in contact with aluminum, gallium can penetrate the grain boundaries. Gallium has a very high X-ray attenuation coefficient compared to aluminum; this renders gallium layers visible by SRCT [28]. Figure 3 shows the superposition of reconstructed tomography images performed on the sample before and after gallium wetting. Coarse precipitates and grain boundaries can clearly be seen owing to the local segregation of gallium. It is observed that both coarse Mg_2Si precipitates and iron-rich intermetallics are mostly distributed on grain boundaries.

The image analysis conducted on tomography data has revealed the Feret diameters [29] of precipitates defined as the diameters derived from the distance of two tangents to the contour of the particle in *L*, *S*, or *T* direction, referred as F_L, F_S, and F_T, respectively. The average values for all precipitates are listed in Table 2. Due to the forging process, these coarse precipitates have a slightly elongated shape (Figure 2).

To analyze the spatial distribution of the particles, the Voronoi diagrams [30] are often used that decompose the threshold image by cells in each of which contains a particle. The particles are assimilated as a point in this method so that the elongated shape of the particles is not taken into account.

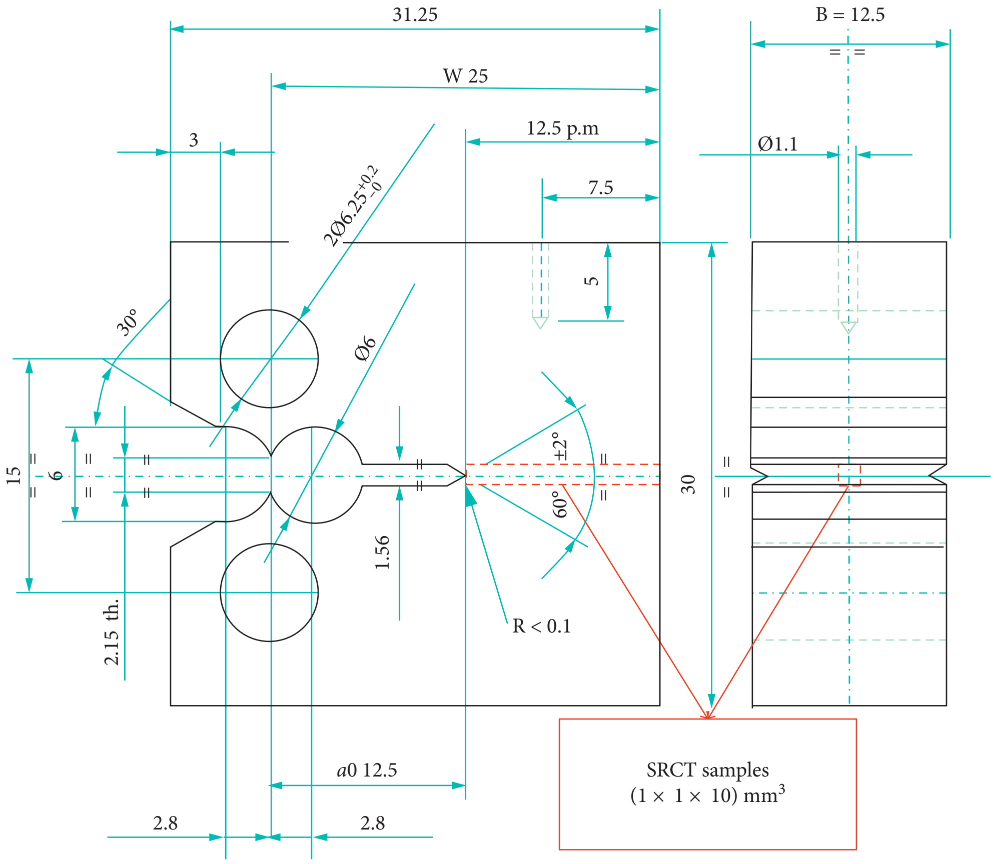

Figure 1: Geometry of CT specimens and position of SRCT samples (red parallelepiped).

In this study, the Voronoi cell diagram is computed on the 3D image by the watershed transform [31, 32] to overcome the limit.

Figures 4(a) and 4(b) show, respectively, 2D sections of Voronoi cells computed by the watershed transform associated with coarse Mg_2Si precipitates and iron-rich intermetallics. The Feret diameters of cells were quantified and are shown in Table 2 for both coarse phases through *L*, *S*, and *T* directions. Alignment of precipitates is shown in Figure 2 through the *L* direction. It is expected that the Voronoi cells are "compressed" along this direction as the interprecipitate distance is smaller in this direction. Nevertheless, this conclusion cannot be drawn for coarse Mg_2Si precipitates, which is probably due to the presence of threshold noises (small objects). This conclusion is however observed for cells of iron-rich intermetallics with a flat shape, which means an alignment of these intermetallics along the *L* direction.

3.2. Tensile Tests on Smooth and Notched Specimens.

Figure 5 shows the results of tensile tests on smooth specimens loaded through *L* and *T* directions. The yield strength (YS) and ultimate tensile strength (UTS) are approximately identical for the two loading directions. The fracture surfaces for both loading directions are spherical, which indicates an isotropic behavior of plasticity. However, the ductility, i.e., fracture strain is significantly different, with specimen loaded through the *L* direction is 3 times higher than that loaded through the *T* direction.

3.3. Toughness Tests.

Figure 6 shows the results of toughness tests for LS and TL configurations in terms of the force as a function of the crack mouth opening displacement (CMOD). The maximum load is higher for the LS configuration (~4.7 kN) as compared to the TL configuration (~3 kN).

3.4. Fractography of CT Specimens.

Fracture surfaces have been analyzed by using the scanning electron microscope (SEM) for specimens on LS and LT configurations (Figure 7). It is found that most zones are covered by dimples at 10 to 30 μm with the presence of Mg_2Si and iron-rich intermetallics (Figure 7(a)), interconnected by submicron dimples or shear zones (Figure 7(b)). Whatever the test configuration, dimples are spherical which means that the growth of cavities is isotropic in the fracture plane.

For the specimen loaded in the TL configuration, the crack propagates through the direction of alignment of coarse precipitates. The fracture mode is primarily intergranular due to the intergranular distribution of coarse precipitates. The absence of transgranular coarse precipitates requires the sudden crack bifurcation during its propagation to join another alignment of intergranular precipitates. This

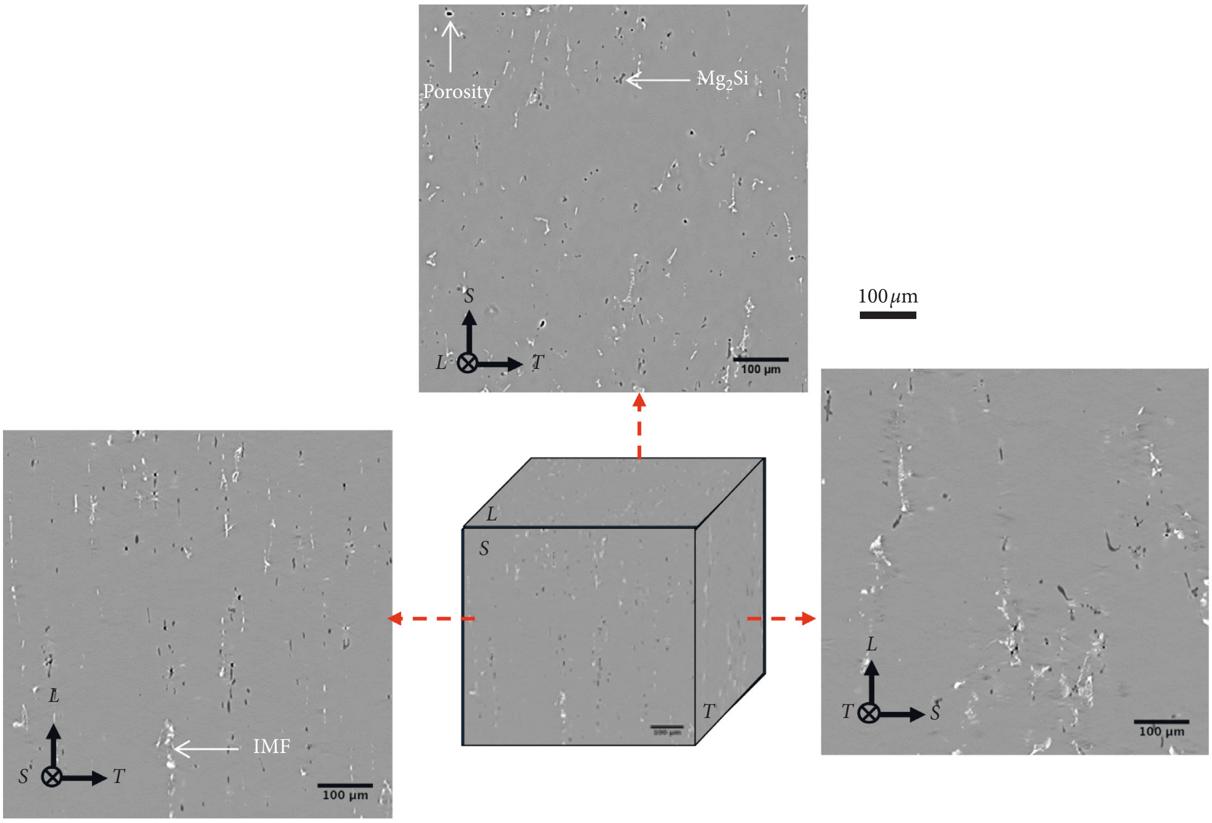

Figure 2: Reconstructed 2D images obtained by SRCT showing the microstructure of the as-received material.

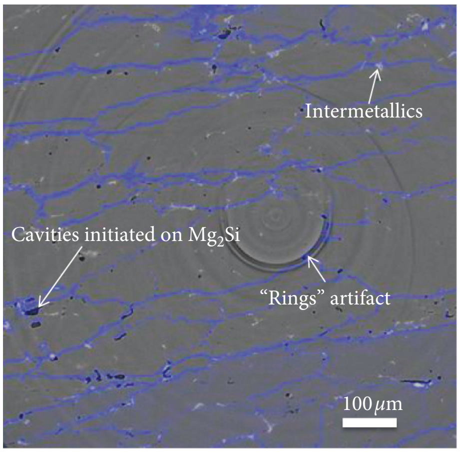

Figure 3: Reconstructed 2D image showing coarse Mg_2Si precipitates, iron-rich intermetallics, and grain boundaries obtained by superposition of tomography images performed on the sample before and after gallium wetting. "Rings" artifact is also visible on the image.

bifurcation is also observed by Achon and Di Russo [33, 34], which occurs along cliffs perpendicular to the propagation plane (Figure 7(a)). Dimples are close to each other and well defined as the void coalescence takes place primarily by internal necking.

In the case of a LS test configuration, crack propagates perpendicular to the plane of alignment of coarse precipitates and therefore gets through grains in their thickness direction. Ductile dimples are smaller connected by smooth areas of a size close to the width of grains (Figure 7(b)). In the smooth area, submicron-sized dimples could be observed with the presence of a second population of precipitates much smaller. The authors showed that this second population of precipitates is probably homogeneously distributed dispersoids of chromium and manganese with a size between 50 nm and 300 nm [35–38]. The fracture mode for the LS configuration is therefore the combination of intergranular and transgranular modes. The primary void coalescence occurs then by shear band with a presence of void sheeting [16].

3.5. SRCT Study of Fracture Mechanism in Interrupted CT Specimens. Tomography scans of interrupted cracks allow observation of the fracture mechanism during the crack initiation and propagation in 3D as well as the subsequent evolution of the fracture process in front of the crack tip. In this study, the CT specimens have been interrupted immediately after the maximum of loads is reached during toughness tests in two configurations (TL and LS) where samples in the crack initiation and propagation region have been taken and observed by SRCT (Figure 1).

Figures 8(a) and 8(b) show the local crack opening map (COD map) of those cracks for TL and LS loading configurations. In both configurations, we distinguish the area of the fatigue precrack region and the ductile crack

TABLE 2: Feret dimensions of coarse precipitates and Voronoi cells through L, S, and T directions. Deviation is estimated to about 25% owing to the threshold uncertainty.

	Mg_2Si			Iron-rich intermetallics		
	F_L (μm)	F_S (μm)	F_T (μm)	F_L (μm)	F_S (μm)	F_T (μm)
Precipitates	8.5 ± 2.1	6.6 ± 1.6	5.2 ± 1.3	8.7 ± 2.1	8.3 ± 2	6.3 ± 1.5
Voronoi cells	94 ± 23	95 ± 23	104 ± 26	67 ± 16	83 ± 20	104 ± 26

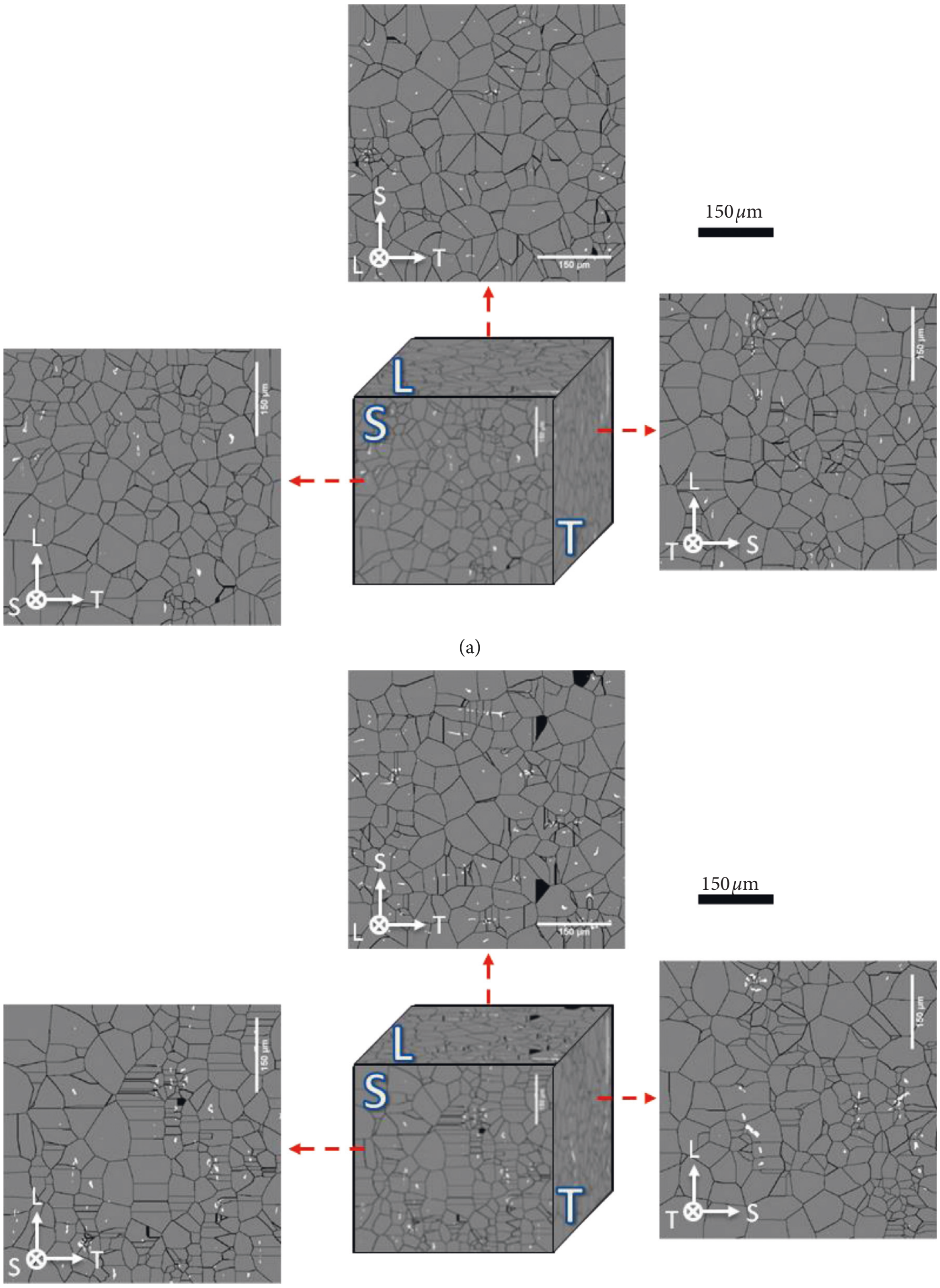

FIGURE 4: Reconstructed 2D images of the Voronoi cells [30] computed by the watershed transform [31, 32] superposed with threshold precipitates: (a) coarse Mg_2Si precipitates; (b) iron-rich intermetallics.

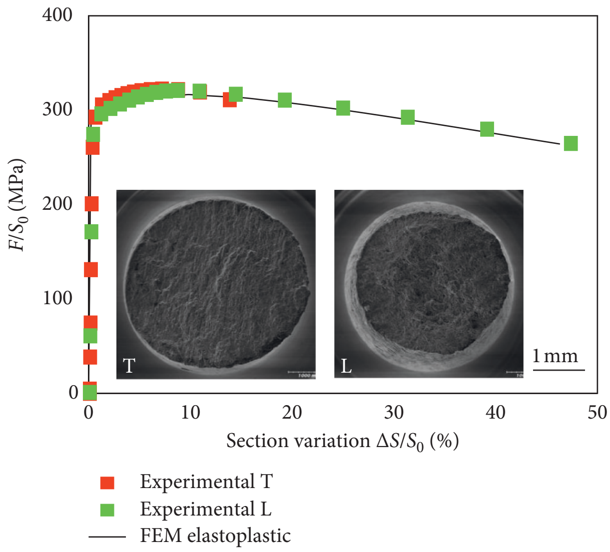

Figure 5: Tensile tests: experimental and simulation with elastoplastic hardening law (FEM).

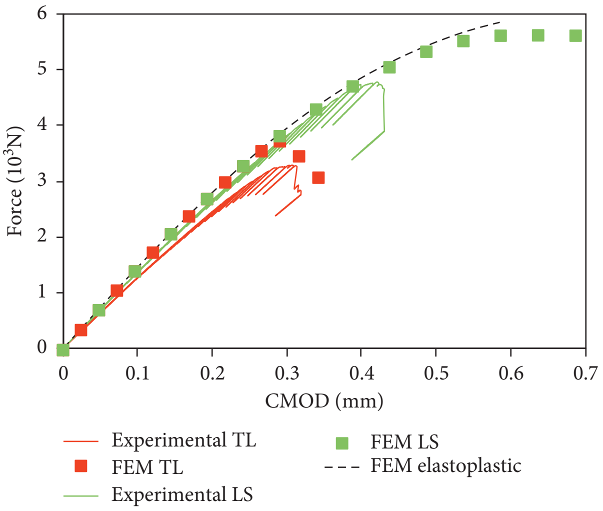

Figure 6: Experimental toughness tests and finite element simulations (FEMs) for configuration LS and TL.

propagation. Only damage percolated with the crack is represented, whereas isolated damage in front of the crack is not shown in the COD map.

In the TL configuration (Figure 8(a)), the crack is continuously formed by spherical dimples with a size related to isolated cavity a head of the crack. The interdamage distance is low (about 50 microns) indicating that coalescence by internal necking is dominant. Some narrow and opened ligaments are also recognized which can be referred to cliffs observed in fracture surfaces (Figure 7(a)).

In the LS configuration (Figure 8(b)), the fatigue precrack is more open than in the TL configuration indicating a better resistance to the crack propagation in this configuration. We note an absence of well defined crack tip. The crack propagation zone is not continuous with the presence of bridges between clusters of cavities.

Figures 9(a) and 9(b) show the 2D sections through white lines in Figure 8. These sections confirm the conclusions obtained in fractography analysis (Figure 7). For TL configuration (Figure 9(a)), the crack propagates parallel to the direction of alignment of coarse precipitates. The failure mode is mainly intergranular. For LS configuration (Figure 9(b)), in addition to the intergranular damage mode, the transgranular narrow ligaments are observed between void clusters.

Figures 9(c) and 9(d) show the 2D sections through green lines in Figure 8. For TL configuration (Figure 9(c)), the crack is continuous with small-coalesced cavities. The void coalescence by internal necking is early and rapid with a very limited void growth stage. For LS configuration (Figure 9(d)), continuous crack propagation is not observed but large clusters of cavities at grain boundaries are linked by narrow ligaments. Void coalescence takes place later by a second population of voids initiated on dispersoids of chromium and manganese [35–38].

Analysis presented in Figure 8 in terms of crack opening displacement is calculated in terms of void volume fraction in regions of interests (ROI) equal to $140 \times 140 \times 70\,\mu\text{m}^3$. Figure 10 shows a map of average void volume fraction in each ROI in the crack propagation plane, the value selected and shown in the figure corresponds to the maximum value in the loading direction (normal to the propagation plane).

Figure 11 illustrates evolution of void volume fraction averaged through width of specimens in function of distance in the crack propagation direction. The two values indicated by arrows represent the average fraction measured at crack tip of the two configurations (dotted lines in Figure 10). The position of the crack tip is chosen at the maximum crack propagation for which all void volume fraction values are nonzero. These values, 1.5% for TL configuration and 5.6% for LS configuration, will be used as critical void volume fraction at failure in the modeling.

4. Modeling

4.1. Parameter Identification. The material model is described in Appendix A including the Voce hardening law [39] and the Gurson–Tvergaard–Needleman (GTN) damage model [5, 6] where the material damage is associated with a void volume fraction. The main material characteristic parameters included in the models are (i) parameters of the hardening law, (ii) preexisting voids and void nucleation parameters, (iii) void growth parameters, and (iv) void coalescence parameters.

The hardening curve is experimentally measured using tensile tests performed on smooth specimens. Beyond uniform elongation of the specimen, the true stress/strain tensile relationship was determined by using the Bridgman correction [40]. The parameters of the isotropic Voce hardening law have been fitted to the experimental data, which leads to the values presented in Table 3. The Voce law only describes stage III. The adjustment of the law is in good agreement with the experimental data (Figure 5). Stage IV could be neglected.

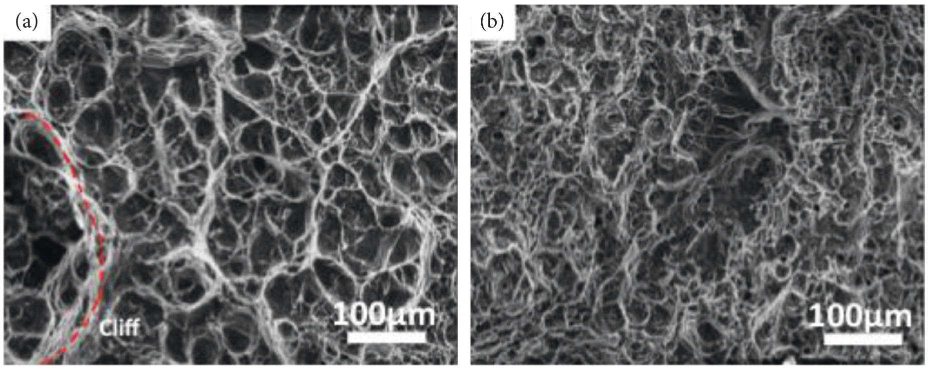

Figure 7: Fracture surfaces of toughness specimens in the crack propagation zone for (a) TL and (b) LS configurations.

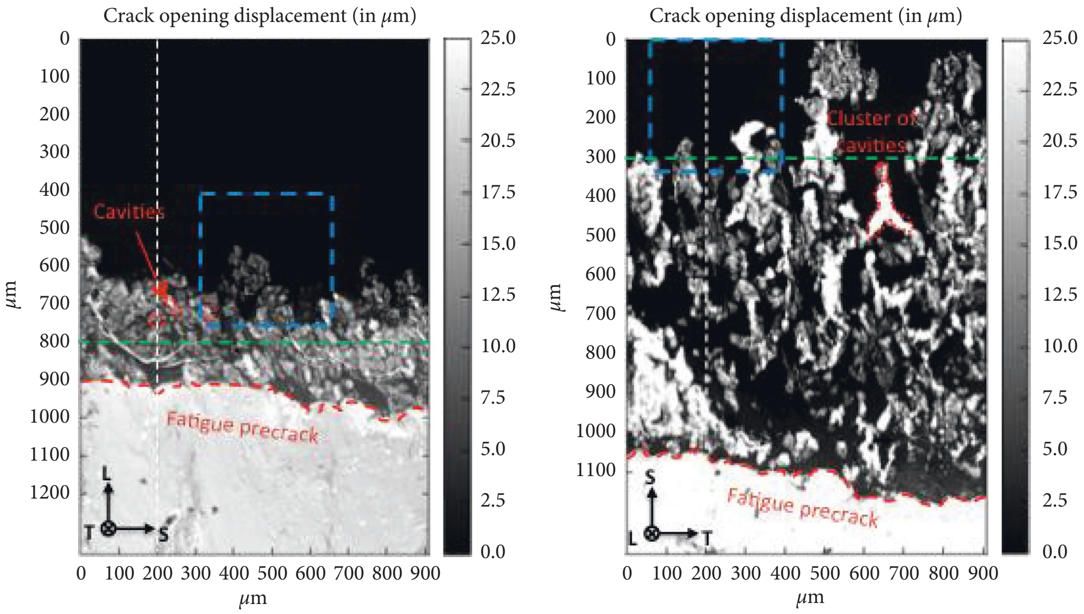

(a)

(b)

Figure 8: Representation of the local crack tip opening via a “sum along ray method” for (a) TL and (b) LS configurations (with lines indicating locations of the 2D sections).

As concluded obviously by synchrotron laminography in situ analysis [9], the coarse Mg_2Si precipitates start to be damaged in the very early loading stage. This has been confirmed in in situ SEM tensile tests (not shown here) where the coarse Mg_2Si precipitates fracture already in the elastic part of the stress-strain curve. As a consequence, these precipitates are considered as preexisting voids f_0 in the simulations.

Cavities nucleating on iron-rich intermetallics are taken into account in the void nucleation parameters. The volume fraction of iron-rich intermetallics obtained by SRCT is considered as the maximum value of the voids that could be nucleated f_n. The two other parameters of the void nucleation law (ε_{n0} and s_{n0}) are determined by fitting the evolution of density of cavities measured by image analysis during in situ SEM tensile tests and the void nucleation law (not presented here).

The values proposed by Tvergaard and Needleman [6] ($q_1 = 1.5$ and $q_2 = 1$) are used as void growth parameters in the GTN model.

The quantitative analysis described in Section 3.5 provides us the critical void volume fraction at failure for both configurations TL and LS. The crack extends over one element when void volume fraction in ROI has reached this critical value $f_f = 1.5\%$ for TL configuration and $f_f = 5.6\%$ for LS configuration throughout the entire element. It is noted that this value is obtained experimentally with an ROI of $140 \times 140 \times 70\,\mu m^3$ in front of the crack. The same element size must be used in finite element analysis, which is $70 \times 70 \times 70\,\mu m^3$ with the symmetry condition around the center of specimen.

For the present material, two reasons lead us to consider that the material loses its strength once the void coalescence begins. First of all, we cannot observe any coalescence

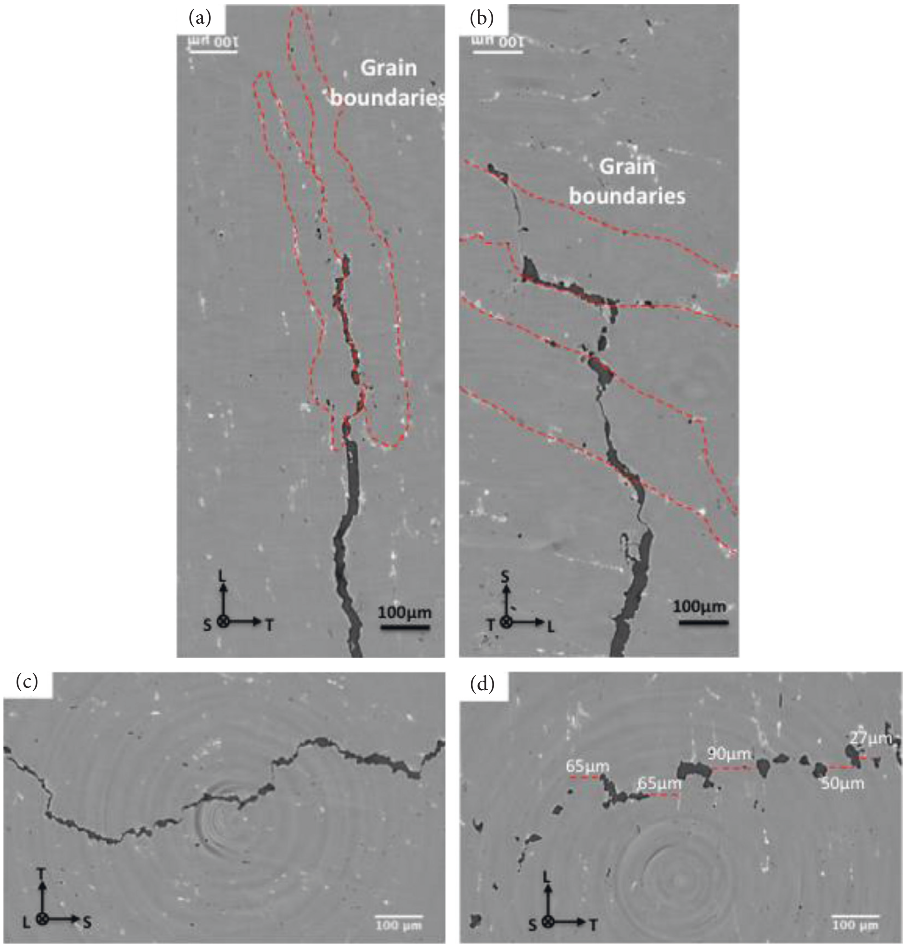

Figure 9: 2D sections of the SRCT data through white lines in Figure 8 for (a) TL and (b) LS configurations as well as through green lines in Figure 8 for (c) TL and (d) LS configurations.

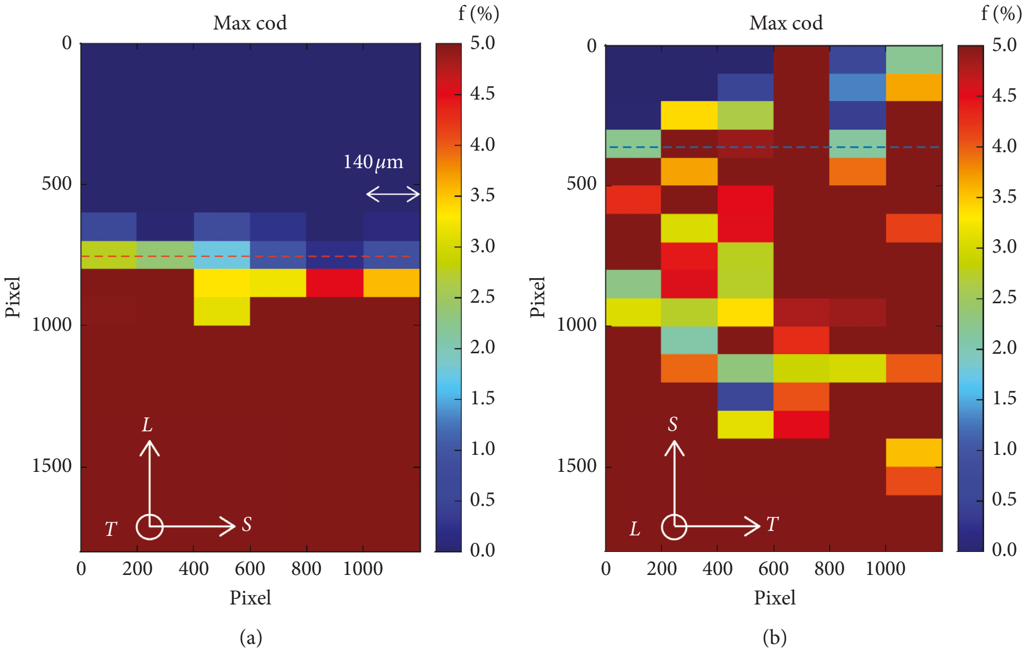

Figure 10: Void volume fraction map in region of interests (ROI) = $140 \times 140 \times 70\,\mu\text{m}^3$ for configurations (a) TL and (b) LS.

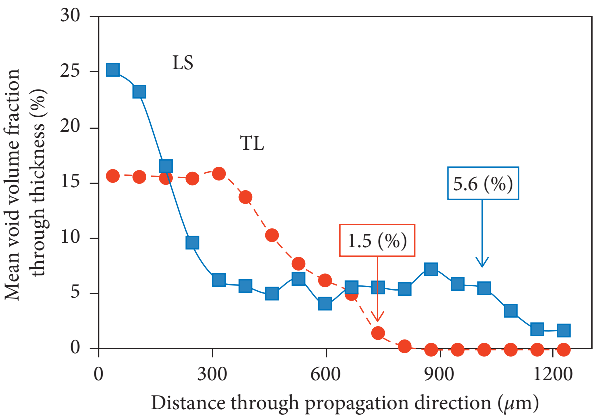

Figure 11: Evolution of mean void volume fraction, averaged through the width of the specimen, in function of the distance in the direction of crack propagation. The two values in red and blue represent the average fraction measured at crack tip (dotted lines in Figure 10).

Table 3: Parameters identified for SRCL finite element simulations.

(i)			(ii) Voce hardening law		
	E in GPa	ν	σ_0 in MPa	σ_s in MPa	b
	70	0.33	288	375	12
(iii)		(iv) Preexisting voids and void nucleation			
	f_0	f_n	ε_{n0}	s_{n0}	
	0.43%	0.59%	10%	0.1	
(v)			(vi) Void growth		
	q_1	q_2			
	1.5	1			
(vii)			(viii) Void coalescence		
	f_c	δ	f_f		
TL	1.5%	∞	1.5%		
LS	5.6%	∞	5.6%		
(ix)			(x) Element sizes		
			$(140 \times 140 \times 140)\ \mu\text{m}^3$		

between voids without involving the crack, which means that the crack begins to propagate at the same time or earlier than void coalescence at the present stress state. Secondly, it was observed previously by ex situ SRCT tensile tests that the damage evolution is extremely rapid after the coalescence has started. Therefore, the critical void volume fraction at coalescence f_c is assumed to be the same as the critical value at which the crack extends f_f, and the acceleration factor $\delta = ((f_u - f_c)/(f_f - f_c))$ is thus infinite.

To sum up, the parameters used for the finite element simulations are resumed in Table 3.

4.2. Model Predictions. The finite-element simulation technique is described in Appendix B. The experimental study showed a strong anisotropy of toughness for the forged AA6061 aluminum alloy. The toughness is significantly lower in TS configuration than in LS configuration. The two configurations have been simulated by using different sets of damage parameters of the GTN model.

Figure 6 shows load-CMOD curves for both experimental results and finite element simulation results for CT specimens in TL and LS configurations. Only the parameters of critical void volume fraction at coalescence and failure are different for the two configurations, i.e., $f_c = f_f = 1.5\%$ for TS configuration and $f_c = f_f = 5.6\%$ for LS configuration.

In the case of TL configuration (red symbols and curve in Figure 6), the maximum load and the opening displacement are well predicted. It should be noted that no parameter is adjusted to obtain a good agreement between simulations and experimental results.

In the case of LS configuration (green symbols and curve in Figure 6), the simulation has overestimated the maximum load because the critical failure parameter $f_f = 5.6\%$ is too high. This can be improved by a more precise identification of the parameters. As we have shown in Sections 3.4 and 3.5, the intergranular and transgranular failure modes coexist in this configuration. Coalescence between void clusters takes place on narrow ligaments across grains involving the nucleation, growth, and coalescence of a second population of precipitates, i.e. dispersoids of chromium and manganese. This second damage mechanism during coalescence of the primary voids is partly neglected in the traditional GTN model.

5. Conclusions

Toughness tests on CT specimens have been carried out in two loading configurations: TL and LS on a forged AA6061 aluminum alloy in T6 condition. The material is highly anisotropic in terms of toughness values with LS configuration larger than TL configuration. Nevertheless, tensile tests performed on smooth specimens reveal an isotropic plastic behavior, which is used to fit an isotropic Voce hardening law. A previous study by in situ synchrotron laminography [9] and fractography of CT specimens have concluded fracture mechanisms linked to coarse precipitates and shear bands. The anisotropy of toughness is due to the anisotropic shape and distribution of coarse precipitates induced by the morphological anisotropy of grains. Anisotropic initial shape and distribution of coarse precipitates have been identified through SRCT studies of the as-received material. SRCT analysis of arrested cracks has revealed different fracture modes for the configurations TL and LS. Voids nucleate first on coarse Mg_2Si precipitates, followed by growth and coalescence. The iron-rich intermetallics enter in this procedure much later. Void coalescence is easier if the coarse precipitates are close to each other. For TL configuration, the coarse precipitates are intergranular and aligned in the plane of crack propagation. Void coalescence takes place by internal necking and the crack propagates mainly by the intergranular failure mode where the fracture energy is lower. For LS configuration, the coarse precipitates are aligned perpendicular to the plane of the crack propagation. Intergranular and transgranular fracture modes coexist in this case and the fracture energy is therefore higher [3, 41]. The void coalescence takes place by internal necking and a second mechanism on a second population of precipitates, i.e., dispersoids of chromium and manganese [35, 38].

The quantitative void volume fraction analysis has been conducted on SRCT data of the arrested cracks for the two configurations. The void volume fraction at crack tip was evaluated at 1.5% for TL configuration and 5.6% for LS configuration for a region of interests of $140 \times 140 \times 70\,\mu\text{m}^3$.

The anisotropic damage mechanism has been validated by the finite element simulations based on the GTN micromechanical damage model with different sets of damage parameters for different configurations. The void volume fraction at crack tip was used as the critical void volume fraction for failure of elements with the same element size. Other parameters were identified by in situ SEM experiments and SRCT microstructural analysis. In this identification procedure, all parameters were identified experimentally by a local approach and in situ observation without parameter adjustment. Finite element simulation conducted on the CT specimens shows the good agreement for TL configuration, whereas the simulation on LS configuration overestimates the maximum load owing to the neglecting of the role of second population of precipitates.

Appendix

A. Material Models

A1. Voce Hardening Law. The plastic hardening is represented by a Voce-type stress saturation equation and is expressed as follows [39]:

$$\sigma = \sigma_s + (\sigma_0 - \sigma_s)\exp(-b\varepsilon), \tag{A.1}$$

where σ_0 is the yielding stress and σ_s and b are the undamaged material constants.

A2. GTN Damage Model. The Gurson–Tvergaard–Needleman (GTN) micromechanical model [5, 6] is used to introduce damage which is represented by a single scalar variable, the void volume fraction f. The plastic flow potential Φ is written as follows:

$$\emptyset = \frac{\sigma_{\text{eq}}^2}{\sigma_{\text{y}}^2} + 2q_1 f^* \cosh\left(\frac{3q_2}{2}\frac{\sigma_m}{\sigma_{\text{y}}}\right) - 1 - (q_1 f^*)^2 = 0. \tag{A.2}$$

The function f^* is the effective porosity and is justified to describe the onset of the void coalescence beyond a critical porosity f_c. The void coalescence is represented by an acceleration of damage rate [6] with

$$f^* = \begin{cases} f, & f < f_c, \\ f_c + \delta(f - f_c), & f \geq f_c, \end{cases} \tag{A.3}$$

where q_1 and q_2 are the void growth parameters involving the yield surface, σ_{y} is the yielding stress of nondamaged material, and $\delta = ((f_u - f_c)/(f_f - f_c))$ is the void coalescence acceleration factor. The material loses its stress carrying capacity at $f = f_f$. In this case, the crack is assumed to propagate.

The evolution of void volume fraction includes two parts: the growth of the existing voids and the nucleation of new voids. The increase of void volume fraction in the model is written as

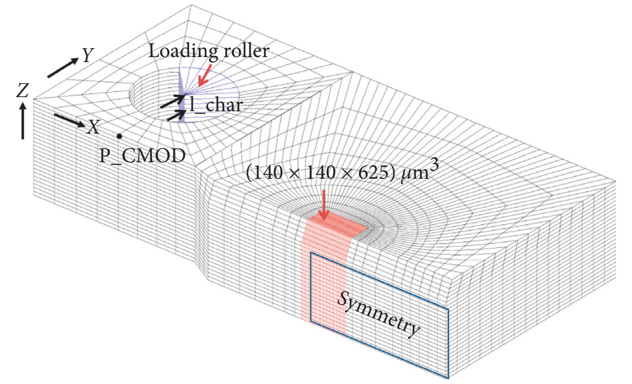

FIGURE 12: 3D mesh of the quarter of the CT specimen with loading roller.

$$\dot{f} = \dot{f}_g + \dot{f}_n. \tag{A.4}$$

Because the matrix material is incompressible, the growth part $\dot{f}_g$ is related to the equivalent plastic strain $\dot{\varepsilon}_{\text{eq}}^p$ and is described as

$$\dot{f}_g = (1 - f)\dot{\varepsilon}_{\text{eq}}^p. \tag{A.5}$$

Chu and Needleman [42] expressed the void nucleation rate by a distribution function considering the heterogeneous nucleation process. This void nucleation law is dependent exclusively on the equivalent plastic strain:

$$\dot{f}_n = A\dot{\varepsilon}_{\text{eq}}^p. \tag{A.6}$$

The coefficient A is selected so that the void nucleation follows a normal distribution function [42] described as

$$A = \frac{f_{n0}}{s_{n0}\sqrt{2\pi}}\exp\left(\frac{1}{2} - \left(\frac{\varepsilon_{\text{eq}}^p - \varepsilon_{n0}}{s_{n0}}\right)^2\right), \tag{A.7}$$

where f_{n0} is the maximum value of nucleated void fraction, ε_{n0} is the mean strain for which the nucleation appears, and s_{n0} represents the deviation of the mean strain for which the nucleation appears.

B. Simulation Technique

The GTN model was implemented in the finite element software Cast3m (http://www-cast3m.cea.fr/), developed by the CEA in France. Due to symmetry, a quarter of the three-dimensional SRCL specimen is meshed by using quadratic elements with reduced integration (Figure 12).

When modeling crack propagation using continuum damage mechanics, the crack is a thin volume which height is half the element height in the case of quadratic elements with reduced integration (type CU20 with 20 nodes and 8 Gauss points) [43]. The mesh is refined in the crack region with element size of about $140 \times 140 \times 140\,\mu\text{m}^3$, which means $70 \times 70 \times 70\,\mu\text{m}^3$ for inter Gauss point size equivalent to the size of ROI in the quantitative experimental analysis in Section 3.5 with respect to the symmetric condition. The loading roller of experimental setup is modeled as a rigid body. The friction is neglected between roller and specimen. Loading is applied via imposed displacement through the Y-axis at line l_char. The same as in the experimental analysis,

$\delta 5$ is calculated at every loading step as twice the displacement of the marker P_$\delta 5$ positioned on the surface of the specimen at 2.5 mm through the Y-axis.

Data Availability

All data used in this article are restricted by the French Atomic Energy and Alternative Energy Commission in order to protect privacy. Requests for data may be considered by the corresponding author for researchers who meet the criteria for access to confidential data under conditions.

Conflicts of Interest

The authors declare that they have no conflicts of interest.

Acknowledgments

The authors would like to thank Pierre Wident and David Leboulch from CEA as well as Henry Proudhon and Frank Nguyen from Centre des Materiaux of Mines ParisTech for technical support.

References

[1] R. S. Alwitt, "The Aluminium-Water System," in *Oxide and Oxide Films*, J. W. Diggle and A. K. Vijh, Eds., Marcel Dekker, New York, NY, USA, 1976.

[2] T. F. Morgeneyer, J. Besson, H. Proudhon, M. J. Starink, and I. Sinclair, "Experimental and numerical analysis of toughness anisotropy in AA2139 Al-alloy sheet," *Acta Materialia*, vol. 57, no. 13, pp. 3902–3915, 2009.

[3] D. Lassance, D. Fabregue, F. Delannay, and T. Pardoen, "Micromechanics of room and high temperature fracture in 6xxx Al alloys," *Progress in Materials Science*, vol. 52, no. 1, pp. 62–129, 2007.

[4] D. Steglich, W. Brocks, J. Heerens, and T. Pardoen, "Anisotropic ductile fracture of Al 2024 alloys," *Engineering Fracture Mechanics*, vol. 75, no. 12, pp. 3692–3706, 2008.

[5] A. L. Gurson, *Plastic Flow and Fracture Behavior of Ductile Materials Incorporating Void Nucleation, Growth and Interaction*, Brown University, Rhode, RI, USA, 1975.

[6] V. Tvergaard and A. Needleman, "Analysis of the cup-cone fracture in a round tensile bar," *Acta Metallurgica*, vol. 32, no. 1, pp. 157–169, 1984.

[7] J. Lemaitre, R. Desmorat, and M. Sauzay, "Anisotropic damage law of evolution," *European Journal of Mechanics-A/Solids*, vol. 19, no. 2, pp. 187–208, 2000.

[8] Y. Hammi and M. F. Horstemeyer, "A physically motivated anisotropic tensorial representation of damage with separate functions for void nucleation, growth, and coalescence," *International Journal of Plasticity*, vol. 23, no. 10-11, pp. 1641–1678, 2007.

[9] Y. Shen, F. T. Morgeneyer, J. Garnier, L. Allais, L. Helfen, and J. Crépin, "Three-dimensional quantitative in situ study of crack initiation and propagation in AA6061 aluminum alloy sheets via synchrotron laminography and finite-element simulations," *Acta Materialia*, vol. 61, no. 7, pp. 2571–2582, 2013.

[10] A. A. Benzerga, J. Besson, and A. Pineau, "Anisotropic ductile fracture," *Acta Materialia*, vol. 52, no. 15, pp. 4623–4638, 2004.

[11] A. A. Benzerga, J. Besson, and A. Pineau, "Anisotropic ductile fracture," *Acta Materialia*, vol. 52, no. 15, pp. 4639–4650, 2004.

[12] M. Gologanu, J.-B. Leblond, G. Perrin, and J. Devaux, "Theoretical models for void coalescence in porous ductile solids. I. Coalescence "in layers"," *International Journal of Solids and Structures*, vol. 38, no. 32-33, pp. 5581–5594, 2001.

[13] T. Pardoen and J. W. Hutchinson, "Micromechanics-based model for trends in toughness of ductile metals," *Acta Materialia*, vol. 51, no. 1, pp. 133–148, 2003.

[14] T. Pardoen and J. W. Hutchinson, "An extended model for void growth and coalescence," *Journal of the Mechanics and Physics of Solids*, vol. 48, no. 12, pp. 2467–2512, 2000.

[15] P. F. Thomason, "A three-dimensional model for ductile fracture by the growth and coalescence of microvoids," *Acta Metallurgica*, vol. 33, no. 6, pp. 1087–1095, 1985.

[16] W. M. Garrison Jr. and N. R. Moody, "Ductile fracture," *Journal of Physics and Chemistry of Solids*, vol. 48, no. 11, pp. 1035–1074, 1987.

[17] F. Bron, J. Besson, and A. Pineau, "Ductile rupture in thin sheets of two grades of 2024 aluminum alloy," *Materials Science and Engineering: A*, vol. 380, no. 1-2, pp. 356–364, 2004.

[18] Y. Shen, J. Garnier, L. Allais, J. Crepin, O. Ancelet, and J.-M. Hiver, "Experimental and numerical characterization of anisotropic damage evolution of forged Al6061-T6 alloy," *Procedia Engineering*, vol. 10, pp. 3429–3434, 2011.

[19] ISO12135, *Metallic Materials—Unified Method of Test for the Determination of Quasistatic Fracture Toughness*, ISO, Geneva, Switzerland, 2002.

[20] W. F. Brown, *Review of Developments in Plane Strain Fracture Toughness Testing*, ASTM International, Philadelphia, WA, USA, 1970.

[21] K. H. Ho and S. T. Newman, "State of the art electrical discharge machining (EDM)," *International Journal of Machine Tools and Manufacture*, vol. 43, no. 13, pp. 1287–1300, 2003.

[22] T. Weitkamp, P. Tafforeau, E. Boller et al., "Parallel-beam imaging at the ESRF beamline ID19: current status and plans for the future," in *Proceedings of the 10th International Conference on Synchrotron Radiation Instrumentation*, R. Garrett, I. Gentle, K. Nugent, S. Wilkins Eds., vol. 1234, p. 83, American Institute of Physics (AIP), Melville, NY,USA, September 2010.

[23] A. Myagotin, A. Voropaev, L. Helfen, D. Hänschke, and T. Baumbach, "Efficient volume reconstruction for parallel-beam computed laminography by filtered backprojection on multi-core clusters," *Journal of Parallel and Distributed Computing*, vol. 22, no. 12, pp. 5348–5361, 2013.

[24] L. Helfen, A. Myagotin, P Mikulik et al., "On the implementation of computed laminography using synchrotron radiation," *Review of Scientific Instruments*, vol. 82, no. 6, article 063702, 2011.

[25] H. Toda, I. Sinclair, J.-Y. Buffière et al., "Assessment of the fatigue crack closure phenomenon in damage-tolerant aluminium alloy byin-situhigh-resolution synchrotron X-ray microtomography," *Philosophical Magazine*, vol. 83, no. 21, pp. 2429–2448, 2003.

[26] T. F. Morgeneyer, M. J. Starink, and I. Sinclair, "Evolution of voids during ductile crack propagation in an aluminium alloy sheet toughness test studied by synchrotron radiation computed tomography," *Acta Materialia*, vol. 56, no. 8, pp. 1671–1679, 2008.

[27] H. Agarwal, A. M. Gokhale, S. Graham, and M. F. Horstemeyer, "Void growth in 6061-aluminum alloy

under triaxial stress state," *Materials Science and Engineering: A*, vol. 341, no. 1-2, pp. 35–42, 2003.

[28] W. Ludwig and D. Bellet, "Penetration of liquid gallium into the grain boundaries of aluminium: a synchrotron radiation microtomographic investigation," *Materials Science and Engineering: A*, vol. 281, no. 1-2, pp. 198–203, 2000.

[29] ISO13322-1, *Particle Size Analysis—Image Analysis Methods–Part 1: Static Image Analysis Methods*, ISO, Geneva, Switzerland, 2004.

[30] G. M. Voronoi, "Nouvelles applications des parametres continus a la theorie des formes quadratiques. Primiere memoire. Sur quelques proprietes des formes quadratiques positives parfaites," *Journal für die Reine und Angewandte Mathematik*, vol. 133, p. 97, 1907.

[31] Q. Wu, F. Merchant, and K. Castleman, *Microscope Image Processing*, Academic Press, Cambridge, MA, USA, 2008.

[32] S. Beucher and C. Lantuejoul, "Use of watersheds in contour detection," in *Proceedings of the International Workshop on Image Processing: Real-Time Edge and Motion Detection/Estimation*, Rennes, France, September 1979.

[33] P. Achon, "Comportement et ténacité d'alliages d'aluminium à haute résistance," Thèse, Ecole Nationale Supérieure des Mines de Paris, Paris, France, 1994.

[34] E. Di Russo, "Microfractographic characteristics and fracture toughness of 7000 and 2000 series aluminium alloys: proposal of a static fracture model," *Metallurgical Science and Technology*, vol. 4, p. 37, 1986.

[35] J. A. Walsh, K. V. Jata, and E. A. Starke Jr., "The influence of Mn dispersoid content and stress state on ductile fracture of 2134 type Al alloys," *Acta Metallurgica*, vol. 37, no. 11, pp. 2861–2871, 1989.

[36] R. H. Stone and J. A. Psioda, "Discussion of "metallurgical factors affecting fracture toughness of aluminum alloys"," *Metallurgical Transactions A*, vol. 6, no. 4, pp. 668–670, 1975.

[37] I. Kirman, "The relation between microstructure and toughness in 7075 aluminum alloy," *Metallurgical and Materials Transactions B*, vol. 2, p. 1761, 1971.

[38] K. C. Prince and J. W. Martin, "The effects of dispersoids upon the micromechanisms of crack propagation in Al-Mg-Si alloys," *Acta Metallurgica*, vol. 27, no. 8, pp. 1401–1408, 1979.

[39] E. Voce, "The relationship between stress and strain for homogeneous deformations," *Journal of the Institute of Metals*, vol. 74, p. 537, 1948.

[40] P. W. Bridgman, *Studies in Large Plastic Flow and Fracture with Special Emphasis on the Effects of Hydrostatic Pressure*, McGraw-Hill, New York, NY, USA, 1952.

[41] T. Pardoen, D. Dumont, A. Deschamps, and Y. Brechet, "Grain boundary versus transgranular ductile failure," *Journal of the Mechanics and Physics of Solids*, vol. 51, no. 4, pp. 637–665, 2003.

[42] C. C. Chu and A. Needleman, "Void nucleation effects in biaxially stretched sheets," *Journal of Engineering Materials and Technology*, vol. 102, no. 3, p. 249, 1980.

[43] F. Bron and J. Besson, "Simulation of the ductile tearing for two grades of 2024 aluminum alloy thin sheets," *Engineering Fracture Mechanics*, vol. 73, no. 11, pp. 1531–1552, 2006.